Journal of Rock Mechanics and Geotechnical Engineering 16 (2024) 1127–1139

Contents lists available at ScienceDirect

Journal of Rock Mechanics and Geotechnical Engineering

journal homepage: www.jrmge.cn

Full Length Article

Modeling of multiphase flow in low permeability porous media: Effect of wettability and pore structure properties

Xiangjie Qin [a], Yuxuan Xia [a], Juncheng Qiao [a], Jiaheng Chen [b], Jianhui Zeng [a], Jianchao Cai [a,*]

[a] National Key Laboratory of Petroleum Resources and Engineering, China University of Petroleum, Beijing, 102249, China
[b] Research Institute of Petroleum Exploration and Development, Beijing, 10083, China

ARTICLE INFO

Article history:
Received 16 February 2023
Received in revised form
20 April 2023
Accepted 15 June 2023
Available online 26 July 2023

Keywords:
Low permeability porous media
Water-oil flow
Wettability
Pore structures
Dual porosity pore network model (PNM)
Free surface model

ABSTRACT

Multiphase flow in low permeability porous media is involved in numerous energy and environmental applications. However, a complete description of this process is challenging due to the limited modeling scale and the effects of complex pore structures and wettability. To address this issue, based on the digital rock of low permeability sandstone, a direct numerical simulation is performed considering the interphase drag and boundary slip to clarify the microscopic water-oil displacement process. In addition, a dual-porosity pore network model (PNM) is constructed to obtain the water-oil relative permeability of the sample. The displacement efficiency as a recovery process is assessed under different wetting and pore structure properties. Results show that microscopic displacement mechanisms explain the corresponding macroscopic relative permeability. The injected water breaks through the outlet earlier with a large mass flow, while thick oil films exist in rough hydrophobic surfaces and poorly connected pores. The variation of water-oil relative permeability is significant, and residual oil saturation is high in the oil-wet system. The flooding is extensive, and the residual oil is trapped in complex pore networks for hydrophilic pore surfaces; thus, water relative permeability is lower in the water-wet system. While the displacement efficiency is the worst in mixed-wetting systems for poor water connectivity. Microporosity negatively correlates with invading oil volume fraction due to strong capillary resistance, and a large microporosity corresponds to low residual oil saturation. This work provides insights into the water-oil flow from different modeling perspectives and helps to optimize the development plan for enhanced recovery.

1. Introduction

Multiphase flow is a common scenario in underground permeable rocks (Zhao et al., 2016; Mascini et al., 2021), which plays an essential role in efficient development of the hydrocarbon resources (Hao et al., 2022), geological storage of carbon dioxide and hydrogen (Hashemi et al., 2021; Zheng et al., 2022), and water infiltration into the soil (Xu et al., 2021a). With depletion of the conventional oil resources in the world, it is necessary to investigate the water-oil flow in low and ultra-low permeability reservoirs to enhance recovery. Reasonable predictive modeling of this process requires a full understanding of displacement mechanisms, such as macroscopic water-oil relative permeability of samples and microscopic residual oil distribution (Cui et al., 2021; Wang and Sun, 2021; Liu et al., 2022a). However, low permeability reservoirs have complex pore-throat systems and rough surfaces, which increase the difficulty of predicting water-oil occurrence and migration mechanisms (Qiao et al., 2022). In addition, the affinity of the solid to fluids (i.e. wettability) and water-oil interactions further affect the flow characteristics (Cai et al., 2021; Bashir et al., 2022). Although great progress has been made in single-phase flow, complex pore structures and wettability continue to challenge the complete description of the water-oil transport process.

Digital rock modeling based on micro-computed tomography (micro-CT) images provides a powerful approach to understanding fluid transport processes (Lin et al., 2021a, 2021b). Compared with experiments using rock samples and microfluidics, this method is time-saving and low-cost (McClure et al., 2021). More importantly, it quantitatively and visually describes actual pore geometry and reasonably resolves complex flow mechanisms (Chen et al., 2021;

* Corresponding author.
E-mail address: caijc@cup.edu.cn (J. Cai).
Peer review under responsibility of Institute of Rock and Soil Mechanics, Chinese Academy of Sciences.

https://doi.org/10.1016/j.jrmge.2023.06.007

Qin et al., 2022). Lattice Boltzmann (LB) and computational fluid dynamics (CFD) methods are commonly used in fluid flow modeling (Carrillo et al., 2022; Liu et al., 2022b; Yan et al., 2022). LB methods are based on the particle algorithm, which solves the discontinuous fluid flow at a more microscopic scale (Zhang et al., 2022a; Wang et al., 2023). Nevertheless, it is difficult to deal with fluids with high viscosity and density ratios. In contrast, CFD methods coupled with interface detection techniques solve fluid flows on meshed models based on the Stokes equation. It assumes that the fluids are continuous and can handle fluids with large density and viscosity ratios (Ambekar et al., 2021; Wang et al., 2021). Commonly used interface detection methods include volume of fluid (VOF), level set, and phase field. A detailed explanation of above-mentioned methods was given in the research of Basirat et al. (2017).

Therefore, the reconstructed three-dimensional (3D) pore system can be used as a geometric model for direct numerical simulation (DNS) of fluid flow. Wang et al. (2022) introduced the Stokes equation and Arbitrary Lagrange-Euler algorithm to simulate the dynamic flow process of water in complex pore spaces and explained the effect of microscopic pore geometry on transport. For multiphase flow, Hu et al. (2018) conducted immiscible displacement with OpenFOAM and investigated the competing effects of wettability and flow rate on invasion processes. Zhao et al. (2019) compared the classical phase field, VOF, and LB multiphase flow simulation results with microfluidic experiments. They concluded that the 3D simulation methods could capture the thin trailing and corner films, but their computation is challenging. Yang et al. (2021) used the VOF method considering wettability and capillary number to simulate the water-oil displacement process and analyze the residual oil distribution. These DNS methods revealed microscopic displacement mechanisms under different contact angles and interfacial tensions. While flow mechanisms in low permeability rocks with narrow pore throat structures are complex, the boundary slip and fluid-fluid interactions should be further considered at such a microscopic scale. Moreover, DNS methods to explain microscopic flow mechanisms are limited by computation and cannot characterize the macroscopic properties of samples, i.e. capillary pressure and relative permeability.

In recent years, upscaled permeability modeling has attracted much attention due to its representative simulation results. The pore network model (PNM) simplifies the actual pore system and preserves the real pore topology (Yang et al., 2019; Zhang et al., 2020; Zhao et al., 2020). Thus, multiphase flow simulations using PNM significantly reduce the computation (Qin et al., 2021; Zhang et al., 2022b). Furthermore, the predicted relative permeability is meaningful when the model size is larger than the representative elementary volume (REV) (Liu and Wang, 2022). Gharbi and Blunt (2012) constructed a PNM based on CT images of carbonatite to carry out quasi-static displacement. They further explored the effects of wettability and pore connectivity on the water-oil relative permeability. However, the sub-resolution pores are widely distributed in low permeability rocks and are difficult to identify due to the limited resolution of CT (Shan et al., 2022). This significantly affects the drainage and water flooding process. Xu et al. (2021b) constructed a multi-scale PNM considering micropores to analyze the effect of micro-links on flow properties. Based on this, the drainage behavior of tight sandstone was evaluated. Besides, deep learning can also be used to predict upscaled permeability, Siavashi et al. (2022) combined a convolutional neural network and continuous-scale simulator to carry out upscaled relative permeability simulation based on the PNM simulation data and obtained satisfactory results. Despite that rapid progress has been made in upscaled permeability modeling, current PNM-based multiphase flows are mostly quasi-static displacement and simplify the complex microscopic flow mechanisms. The microscopic scenarios, e.g. fingering and residual fluid distribution, cannot be reasonably explained.

Different modeling perspectives can perhaps complement each other to comprehensively describe the water-oil flow in low permeability rocks. This work introduces microscopic and macroscopic models for water-oil flow according to REV analysis. Next, a free surface model considering the interphase drag and boundary slip is developed to visualize the microscopic dynamic water flooding process, and a dual porosity PNM is constructed considering the resolution pores and micropores to obtain the macroscopic relative permeability of the sample. Finally, the effects of wettability and pore structure properties (i.e. micropores and pore-throats) on water-oil flow are analyzed for enhanced oil recovery.

2. Digital rock construction

2.1. CT experiment and image processing

The sandstone sample with a permeability of 1.48 mD from the Dagang Oilfield in Tianjin, China was used for the micro-CT experiment through a Zeiss 500 high-resolution scanner. The sample was first polished and fixed on the stage. Then X-rays were emitted from the radiation source to capture the internal information of the sample, and the information was converted on the detector during scanning (see Fig. 1a). As a result, a total of 1001 two-dimensional (2D) slices with a resolution of 4.7 μm were obtained. It is found that the gray value of the images decreases gradually outward along the sample radius, which leads to the dark image edges (see Fig. 1b). To solve this problem, beam hardening correction was performed before reconstruction. The rotation axis was defined to determine the radial gray distribution of the image, and Gaussian filtering was introduced to smooth the image and normalize it. All the intensities will be divided by this smoothed profile to give a more or less radial averaging. The axial gray value distribution of the processed image was uniform. Moreover, to optimize the image memory and preserve grayscale details, the original 16-bit images were converted to 8-bit, and the grayscale values are distributed between 0 and 255.

Seven hundred images were selected from the intermediate region of the sample and cropped to the size of 700^3 voxels for subsequent analysis. The median filter algorithm was applied to eliminating the influence of randomly distributed noise in images on the reconstruction (see Fig. 1c). Unfortunately, a majority of micropores cannot be observed by micro-CT due to the limitation of resolution. These micropores are generally distributed around the pore spaces and exist in low-density minerals, e.g. clay. Their gray values are slightly higher than that of the pore bodies. In particular, micropores enhance connectivity and have an important impact on water-oil displacement behavior. A developed top-hat segmentation method was used to combine interactive thresholding to segment grayscale images into three phases: resolution pores, micropores, and skeleton (see Fig. 1d). The top-hat segmentation method extracts target structures according to the image brightness, which can reasonably identify tiny pore-fracture structures. However, it is not suitable for large pore-fractures. In contrast, the interactive threshold method is based on the gray value, which accurately identifies large pores and makes up for this defect. Thus, the resolution pores were first conservatively extracted using interactive thresholding, and then superimposed using top-hat segmentation to add tiny pore-fractures. In addition, the skeleton was extracted using interactive thresholding, and the undefined parts of the images were defined as micropores. To ensure the accuracy of reconstruction, the porosity of the reconstructed model was compared with the mercury injection porosity (Idowu et al.,

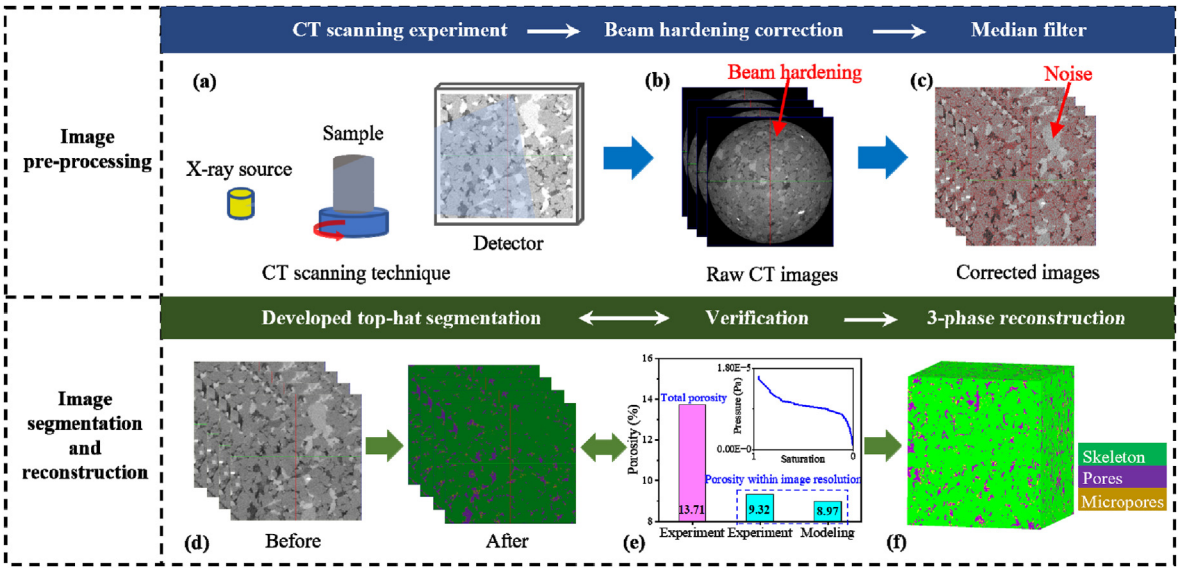

Fig. 1. Image processing and reconstruction process: (a) Principle of micro-CT experiment; (b) Beam hardening; (c) System noise of the images; (d) Image segmentation; (e) Reconstruction accuracy verified by mercury injection porosity; and (f) Three-phase reconstruction of resolution pores, micropores, and skeleton.

2015). The mercury injection porosity of the sample is 13.71%, and the porosity within the certain pore diameter range is 9.32%, which basically corresponds to the reconstruction results (see Fig. 1e). In this way, the digital rock was established for subsequent modeling (see Fig. 1f).

2.2. Model reconstruction based on REV analysis

It is known that the pore system of cropped models is similar and can be used to represent the physical properties of the scanned sample when the model size is larger than the REV. However, the pore system of cropped models differs significantly and reflects pore heterogeneity when the model size is smaller than the REV. Therefore, REV analysis was performed on the scanned sample using resolution porosity (see Fig. 2a). It shows that the porosity between the models is significantly different when the size is less than 260^3 voxels. In contrast, the difference between the models is smaller when the model size is larger than 260^3 voxels. Thus, the porosity-based REV of the sample is 260^3 voxels. Models larger than the REV (i.e. 260^3 voxels) are defined as macroscopic models, which represents the properties of the scanned sample. However, the heterogeneous pore system will be simplified in numerical modeling due to the large model size, and this ignores some microscopic displacement behaviors (Chen et al., 2022). In this case, models smaller than the REV are defined as microscopic models. The complex pore system and microscopic flow mechanisms are fully considered in subsequent modeling due to the smaller model size. This complements the transport behaviors that cannot be revealed by macroscopic models. Fig. 2b illustrates the construction of microscopic and macroscopic models of the scanned sample.

3. Modeling of water-oil flow

The microscopic modeling visualizes the dynamic water-oil displacement process and displays the water-oil distribution in pore-throat networks. For the macroscopic, relative permeability describes the averaged water-oil flow behavior of scanned samples and is universally used in large-scale flow predictions. More importantly, the observed microscopic wetting and displacement mechanisms may seriously affect the macroscopic relative permeability performance.

3.1. Free surface model for microscopic dynamic water-oil flow

A free surface model within the Eulerian-Eulerian two-phase flow model for immiscible continuous fluid is introduced to simulate the microscopic dynamic water flooding process. Compared with other Eulerian-Eulerian methods (VOF and mixture

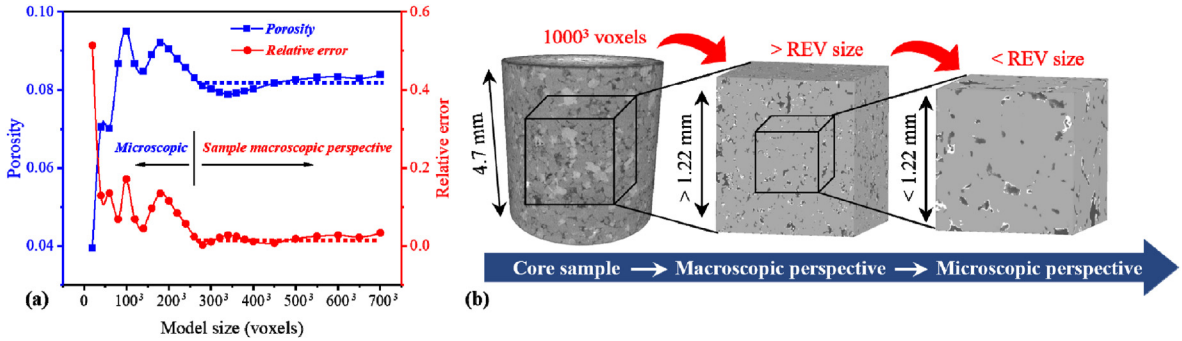

Fig. 2. Construction of microscopic and macroscopic models: (a) Porosity-based REV analysis, and (b) Construction process of the models.

models), it simulates multiphase flow with a complex interface and solves the velocity field and volume fraction of each fluid. Therefore, this method reasonably models the boundary slip of fluids and the entrainment of non-wetting fluids within wetting fluids. While the amount of computation is severely limited due to the complex mechanisms considered in the simulation.

As displayed in Fig. 3a, the model size was determined as 100 × 100 × 120 voxels since the large-scale model is computationally expensive. The pore geometry was meshed to generate high quality grids with the maximum cell size of 9.4 μm. The model contains 120,548 points, 861,411 triangles, and 375,312 tetras (see Fig. 3b). The initial pore system was saturated with oil. The wettability was defined using contact angles, and the contact angles under water-wet and oil-wet conditions were defined as 40° and 110°, respectively (see Fig. 3c). The boundary slip was considered in the simulation; i.e. the wall in contact with the wetting fluid was defined as no slip wall due to the affinity of pore surfaces, and the wall in contact with the non-wetting fluid was free slip wall. The viscosity of water and oil was set to 0.001 Pa s and 0.019 Pa s (Ju et al., 2020). A fixed pressure gradient of 60 kPa was set between the inlet and outlet. The simulation was completed on the ANSYS platform. The following are the principles involved in multiphase flow modeling.

3.1.1. Hydrodynamic equations

The inhomogeneous multiphase flow contains momentum, continuity, and volume conservation equations. The momentum equation for the water-oil flow in pore spaces is

$$\frac{\partial}{\partial t}(\varphi_\alpha\rho_\alpha\boldsymbol{U}_\alpha)+\nabla[\varphi_\alpha(\boldsymbol{U}_\alpha\otimes\boldsymbol{U}_\alpha)]=-\varphi_\alpha\nabla p+\nabla\left[\varphi_\alpha\mu_\alpha\left(\nabla\boldsymbol{U}_\alpha+\nabla\boldsymbol{U}_\alpha^{\mathrm{T}}\right)\right]+\sum_{\beta=1}^{N}\left(\Gamma_{\alpha\beta}^{+}\boldsymbol{U}_\beta-\Gamma_{\alpha\beta}^{+}\boldsymbol{U}_\alpha\right)+\boldsymbol{S}_\alpha+\boldsymbol{M}_\alpha \tag{1}$$

where φ_α is the volume fraction of phase α; ρ_α and μ_α are the density and viscosity of phase α, respectively; t is the computation time; $\boldsymbol{S}_\alpha$ is the momentum source; $\boldsymbol{M}_\alpha$ is the interfacial forces acting on phase α; T is the thermodynamic temperature; $\boldsymbol{U}_\alpha$ and $\boldsymbol{U}_\beta$ are the vector velocity of phase α and phase β, respectively; p is the fluid pressure; N is the total number of phases; $\Gamma_{\alpha\beta}^{+}$ is the positive mass flow rate per unit volume from phase α to phase β; and ∇ is the vector operator.

The fluid flow in pore spaces also satisfies the continuity equation as

$$\frac{\partial}{\partial t}(\varphi_\alpha\rho_\alpha)+\nabla(\varphi_\alpha\rho_\alpha\boldsymbol{U}_\alpha)=\boldsymbol{S}_{s\alpha}+\sum_{\beta=1}^{N}\Gamma_{\alpha\beta} \tag{2}$$

where $\boldsymbol{S}_{s\alpha}$ is the specified mass source, and $\Gamma_{\alpha\beta}$ is the mass flow rate per unit volume from phase α to phase β.

The sum of the volume fractions is 1 (see Eq. (3)), and combine with Eq. (2), divided by phasic density, and sum over all phases to obtain the transported volume conservation equation (see Eq. (4)).

$$\sum_{\alpha=1}^{N}\varphi_\alpha=1 \tag{3}$$

$$\sum_{\alpha}\frac{1}{\rho_\alpha}\left[\frac{\partial}{\partial t}(\varphi_\alpha\rho_\alpha)+\nabla(\varphi_\alpha\rho_\alpha\boldsymbol{U}_\alpha)\right]=\sum_{\alpha}\frac{1}{\rho_\alpha}\left(S_{s\alpha}+\sum_{\beta=1}^{N}\Gamma_{\alpha\beta}\right) \tag{4}$$

3.1.2. Fluid-fluid interactions

The surface tension force was modeled as a volume force on the water-oil interface through a continuum surface force model proposed by Brackbill et al. (1992). Fig. 3c is the water-oil interface. Water is defined as primary fluid α, and oil is defined as secondary fluid β, then the surface tension force $\boldsymbol{F}_{\alpha\beta}$ given by the continuum surface force model is

$$\boldsymbol{F}_{\alpha\beta}=\boldsymbol{f}_{\alpha\beta}\delta_{\alpha\beta} \tag{5}$$

$$\boldsymbol{f}_{\alpha\beta}=\gamma(\nabla_s-k_{\alpha\beta}\boldsymbol{n}_{\alpha\beta}) \tag{6}$$

where γ is the interfacial tension, $\boldsymbol{f}_{\alpha\beta}$ is the net surface force on the element, $\delta_{\alpha\beta}$ is the interface delta function, $\boldsymbol{n}_{\alpha\beta}$ is the interface normal vector, ∇_s is the gradient operator on the interface, and $k_{\alpha\beta}$ is the surface curvature defined by

$$k_{\alpha\beta}=\nabla\boldsymbol{n}_{\alpha\beta} \tag{7}$$

Wall adhesion was considered using a contact angle for the interface between water-oil intersecting a wall. The interface normal vector used for calculating both curvature and the surface tension force must satisfy the wall contact angle. The interfacial transfer was modeled using a mixture model, which is an algebraic prescription for the interfacial area density. The mixture model treats both phases α and β symmetrically. The surface area $A_{\alpha\beta}$ per unit volume is

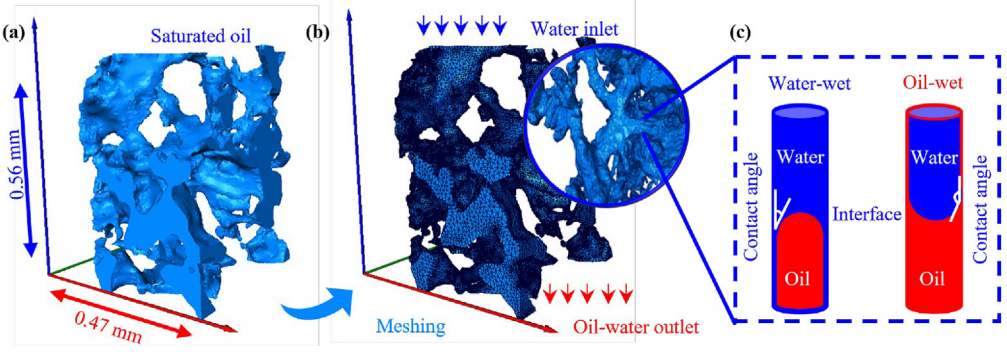

Fig. 3. Microscopic modeling of water flooding: (a) Reconstructed pore geometry; (b) Meshed model; and (c) Water-oil distribution in the water-wet and oil-wet capillary at equilibrium.

$$A_{\alpha\beta} = \frac{\varphi_\alpha \varphi_\beta}{d_{\alpha\beta}} \tag{8}$$

where $d_{\alpha\beta}$ is the interfacial length scale.

A non-dimensional drag coefficient C_D was defined to describe the interphase movement transfer:

$$\boldsymbol{D}_{\alpha\beta} = C_D \rho_{\alpha\beta} A_{\alpha\beta} |\boldsymbol{U}_\beta - \boldsymbol{U}_\alpha| (\boldsymbol{U}_\beta - \boldsymbol{U}_\alpha) \tag{9}$$

where $\boldsymbol{D}_{\alpha\beta}$ is the total drag exerted by phase α on phase β per unit volume, and $\rho_{\alpha\beta}$ is the mixture density.

3.2. Dual-porosity PNM for macroscopic water-oil relative permeability

The PNM was constructed to obtain macroscopic properties of the sample (i.e. relative permeability and capillary pressure), and the dynamic displacement process was ignored. To obtain representative simulation results, the model size was determined to be 600^3 voxels, corresponding to the actual size of 2.82 mm^3. Therefore, a quasi-static method was chosen to simulate water-oil relative permeability, which assumes that capillary forces dominate the fluid flow, and the capillary number is less than 10^{-4}. Resolution and sub-resolution pores (i.e. micropores) compose the model porosity. The influence of micropores on water-oil flow was considered by setting the microporosity of the micropore phase. The wettability of the pore-throat system was defined using the oil-wet pores fraction, including water-wet (i.e. 0), oil-wet (i.e. 1), and mixed-wet (i.e. greater than 0 and less than 1).

3.2.1. PNM extraction

A grain-based approach was used to extract pore skeleton lines. Grains are expanded along the center of pore spaces based on a 3D dilation algorithm, and different grains would contact in the pore space to form skeleton lines. Nodes on the skeleton lines represent pore centers, connections between nodes represent throats, and the number of connections is the coordination number. Fig. 4a illustrates the equivalent pore-throat structures. The maximum internal contact radius of the pore space is defined as the pore radius, and the minimum internal contact radius between two pores is defined as the throat radius. Considering the complex pore-throat shapes, the wetting phase may be trapped in corners during displacement, resulting in altered wettability. Thus, the pore-throat shape is described using a cross-section shape factor G given by

$$G = A/P^2 \tag{10}$$

where A is the pore-throat cross-sectional area, and P is the perimeter of the cross-section. The maximum shape factor value is 0.5, corresponding to a circle. The shape factor of an equilateral triangle is 0.481, and the smaller the shape factor, the more complex the shape.

3.2.2. Fluid flow in quasi-static PNM

Fig. 4b displays the generated PNM. The water-oil flow in the PNM is divided into two stages: drainage and water flooding. As shown in Fig. 4c, the initial pore-throat system is water-saturated and water-wet. Oil invades the pore network under the threshold capillary pressure (see Eq. (11)). During which, the water film on pore-throat surfaces prevents the oil from contacting the wall. The pore-throat system remains water-wet for the active molecules in the oil cannot contact pore-throat surfaces when the invading capillary pressure is less than the threshold capillary pressure for water film rupture. When the invading capillary pressure is greater than the threshold capillary pressure, the water film breaks, the oil contacts the wall, and the pore-throat system changes from water-wet to oil-wet. The pore corners may remain water-wet due to the thick water film. Therefore, the pore-throat system may present three wetting states after drainage, i.e. water-wet, mixed-wet, and oil-wet. The water flooding mechanisms are complicated due to the altered wettability, and water first invades water-wet pore-throat structures during flooding. The mechanisms of water flooding are divided into three types: piston type, pore body filling, and snap-off. The following briefly introduces the principle of PNM for water-oil flow. Detailed information can be found in the publications of Øren et al. (1998) and Hu et al. (2020).

The threshold capillary pressure P_c for primary drainage is determined by pore shape and contact angle (Øren et al., 1998) as

$$P_c = \frac{\gamma\left(1 + 2\sqrt{\pi G}\right)\cos\theta}{r} F(\theta, G) \tag{11}$$

where r is the maximum inscribed circle radius of the pore or throat, θ is the contact angle, and function F is related to the contact angle and shape factor.

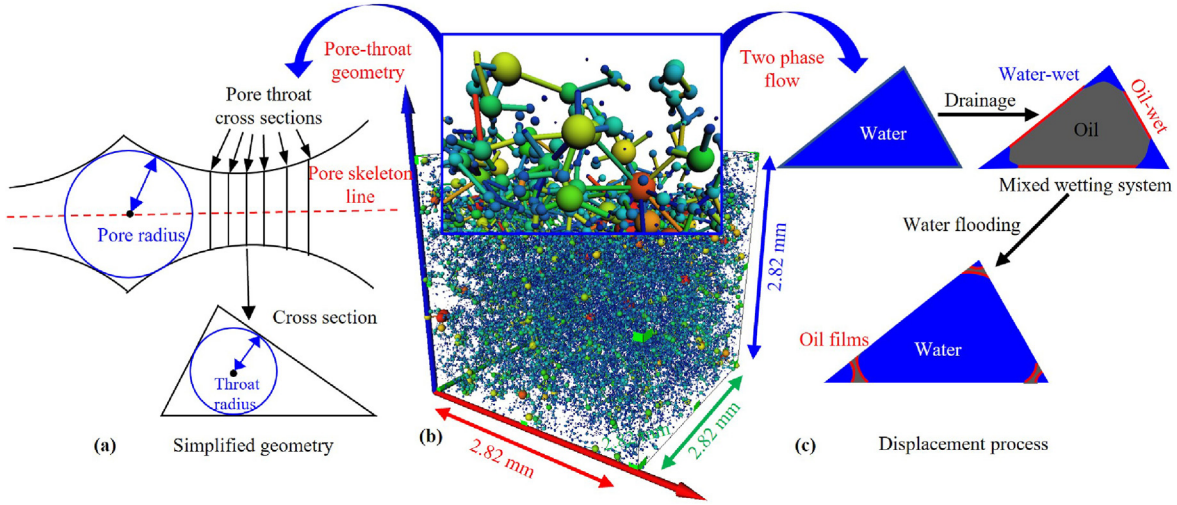

Fig. 4. Description of water-oil flow in PNM: (a) Simplified pore-throat structure; (b) Constructed PNM; and (c) Water-oil displacement process.

The capillary pressure for pore body filling is controlled by the maximum curvature radius, which is determined by the number of oil-filled throats. If there is only one oil-filled throat (i.e. I_1 event), the pore filling process is similar to piston type invasion. For the remaining pore-filling events (i.e. I_2–I_n), the threshold capillary pressures are more complex. The model used is similar to a parametric model presented by Blunt (1997):

$$R_n = \frac{1}{\cos\theta}\left(r_p + \sum_{i=1}^{n} b_i r_i x_i\right) \tag{12}$$

where R_n is the mean radius of curvature for filling by an I_n event, r_p is the pore body radius, b_i is the input parameters, r_i is the radius of the oil filled throat i, and x_i is random numbers between zero and one.

The flow mode in the pore-throat system is laminar, and the flow rate q of each fluid phase between pores a and b is

$$q = \frac{g}{L}(p_a - p_b) \tag{13}$$

where L and g are the distance and effective conductance between pores a and b, and p_a and p_b are the phase potential.

The fluids are incompressible at each pore body; thus, the fluid flow rate of every pore i follows the mass conservation:

$$\sum_j q_{ij} = 0 \tag{14}$$

where j includes all the throats connected to the pore i, and q_{ij} is the flow rate of the pore i contributed by throat j.

In this model, the densities of water and oil are 1000 kg/m^3 and 800 kg/m^3, respectively. The water-oil interfacial tension is 0.048 N/m. The contact angles of the water-wet and oil-wet pore-throat surfaces range from 40° to 60° and 110°–130°. The fluid parameters of each phase including saturation, flow rate, and capillary pressure, were recorded at different stages of displacement, and the absolute and relative permeability values were obtained by Darcy's law.

4. Results and discussion

4.1. Pore structure properties

The resolution pores, micropores, and skeleton structures of the microscopic and macroscopic models of the scanned sample were obtained by image processing technique. The corresponding PNMs were constructed to obtain pore-throat size distribution, including two microscopic models with the sizes of 100^3 and 200^3 voxels, and a macroscopic model with a size of 600^3 voxels. The parameters are shown in Table 1, indicating that the pore system of the 100^3 voxel model is significantly different from that of the 200^3 and 600^3 voxel models due to its large porosity, pore-throat size, as well as the strong pore connectivity. In contrast, the porosity and pore-throat size of the 200^3 and 600^3 voxel models are similar because their dimensions are close to or greater than REV. Figs. 5 and 6 display the structures and pore-throat size distribution of the 200^3 and 600^3 voxel models. Micropores are mainly distributed around the pore space and even connect to the adjacent pores, which enhances pore connectivity. It can be found that the established PNMs correspond to the spatial distribution of resolution pores and micropores. The generated spheres fill pore spaces, and the size corresponds to the pore volume.

Table 1
Parameters of different models with microporosity of 0.5.

Model size (voxels)	Total porosity	Micro porosity	Percolating porosity	Mean pore radius (μm)	Mean throat radius (μm)	Mean coordination number
100^3	0.1127	0.0059	0.0925	10.0269	7.2741	2.1507
200^3	0.0981	0.0062	0.0686	8.3228	6.5987	1.623
600^3	0.0897	0.0059	0.0705	8.4525	6.6638	1.7006

Fig. 6a indicates that the pore volume contribution increases first and then decreases slowly with increasing pore radius; pores with a radius of 10–20 μm contribute more to total pore volume. Besides, the coordination number increases, and the shape factor decreases with increasing pore radius, which indicates that large pores correspond to complex shapes and strong connectivity. From Fig. 6b, the throat number and volume are mainly contributed by the throats with a radius of 0–10 μm; then, the throat number and volume contribution gradually decrease with increasing throat radius. In addition, the throat radius is roughly inversely related to the shape factor. Obviously, the pore-throat distribution of the macroscopic model has strong regularity. In contrast, the shape, size, and connectivity of large pore-throats are randomly distributed in the microscopic model, which is the main reason for the microscopic heterogeneity of rocks. Therefore, the dynamic water flooding simulation carried out on the microscopic model clarifies displacement mechanisms in heterogeneous pore systems; the relative permeability simulation performed using the macroscopic model represents the averaged water-oil flow of the scanned sample.

4.2. Microscopic modeling for dynamic water-oil displacement process

The dynamic flooding process was simulated under water-wet and oil-wet conditions using the method in Section 3.1. After calculation, the solution achieved convergence for the residual of momentum and mass is bellow 10^{-5}. In this way, the influence mechanisms of wettability and pore-throat structures on water flooding were obtained.

The injected water is driven by pressure into the pore-throat system and forms three flow channels. It is found that water displaces oil along pore surfaces under the water-wet condition, while there are thick oil films on pore-throat surfaces under the oil-wet condition, which causes water entrained in the oil (see Figs. 7a and 8a). Accordingly, the flooding process can be divided into three stages based on the water-oil distribution. The variation of water saturation with displacement time is displayed in Figs. 7b and 8b. At the initial flooding stage, the water saturation in the water-wet system is larger due to the positive effect of capillary pressure. After the calculation of first time interval, water volume fractions in the water-wet and oil-wet systems are 10.43% and 10.09%, respectively. Before 1 ms, the water volume fraction is larger in the water-wet system. At the second stage, water continuously invades the pore-throat system, gradually forms dominant displacement channels, and breaks through the outlet. Under the water-wet condition, the first displacement channel is formed at about 5 ms, with a water saturation of 19.86%. Then a second displacement channel is formed at 25 ms, and the third narrow flow channel has been formed at 45 ms, corresponding to the water saturation of 54.21%. In contrast, the water displacement channel is formed earlier under the oil-wet condition. At 5 ms, the injected water has broken through the outlet along the first channel. Especially at 25 ms, three displacement channels have been formed with a water saturation of 49.62%, and the water saturation reaches 58.45% at 45 ms, which is significantly higher than that under the water-wet condition. At the final stage, the increasing

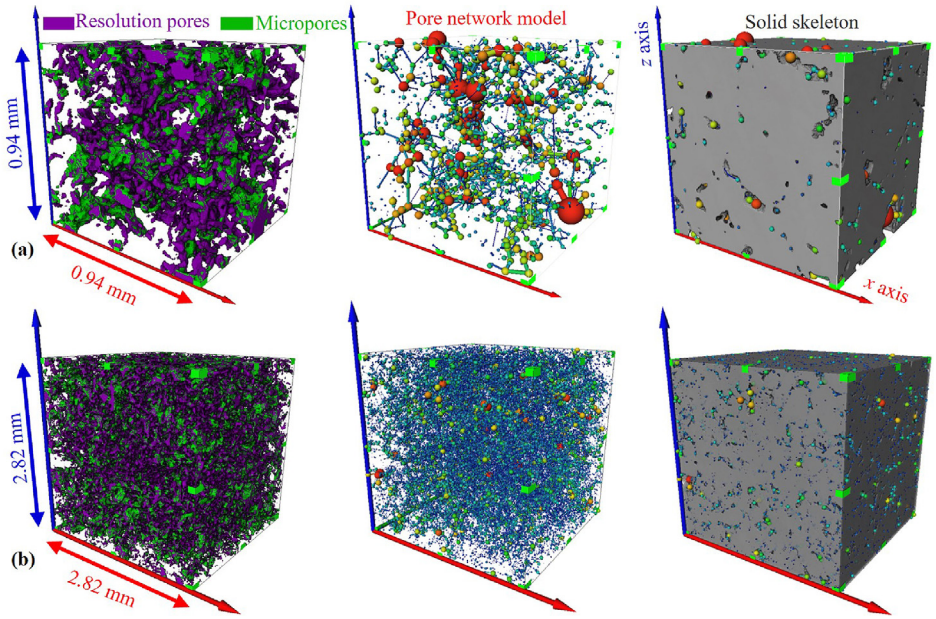

Fig. 5. Structures of macroscopic and microscopic models: (a) Macroscopic model with a size of 600^3 voxels; and (b) Microscopic model with a size of 200^3 voxels.

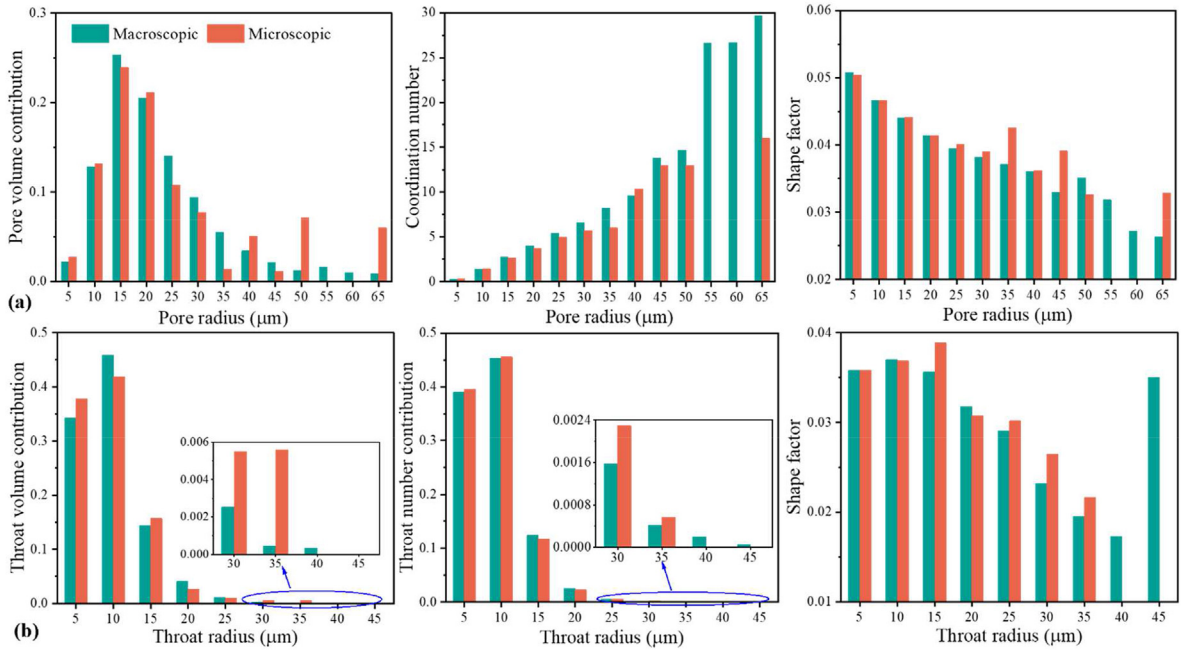

Fig. 6. Pore-throat distribution of microscopic and macroscopic models: (a) Pore size distribution; and (b) Throat size distribution.

rate of water volume fraction decreases as the water has reached the outlet, and the displacement gradually tends to equilibrium.

The corresponding water-oil mass flow during flooding is extracted (see Figs. 7c and 8c). At the beginning of flooding, the oil mass flow is larger in the water-wet system, indicating that water easily enters the water-wet pore-throats and displaces the oil for the hydrophilic surfaces. Subsequently, water mass flow increases slowly, while oil mass flow fluctuates and gradually decreases under the water-wet condition. This indicates that the hydrophilic pore surfaces restrict the water flow; the water-oil interface is complicated and even traps oil in complex pore networks under the influence of positive capillary pressure; at the same time, the oil attached to rough pore surfaces and tiny pores is easily replaced. In contrast, the water mass flow increases rapidly, and the oil mass flow decreases under the oil-wet condition, meaning that hydrophobic pore surfaces facilitate the water flow; besides, the water-oil mass flow curves are smooth, indicating a simple water-oil interface. After the water breaks through the outlet, the variation of water-oil mass flow curves decreases, and oil is slowly displaced by interphase drag under the oil-wet condition. While the water-oil mass flow curves still vary significantly under the water-wet condition, it indicates that a certain amount of oil is displaced by imbibition, and water flooding takes a long time to reach equilibrium.

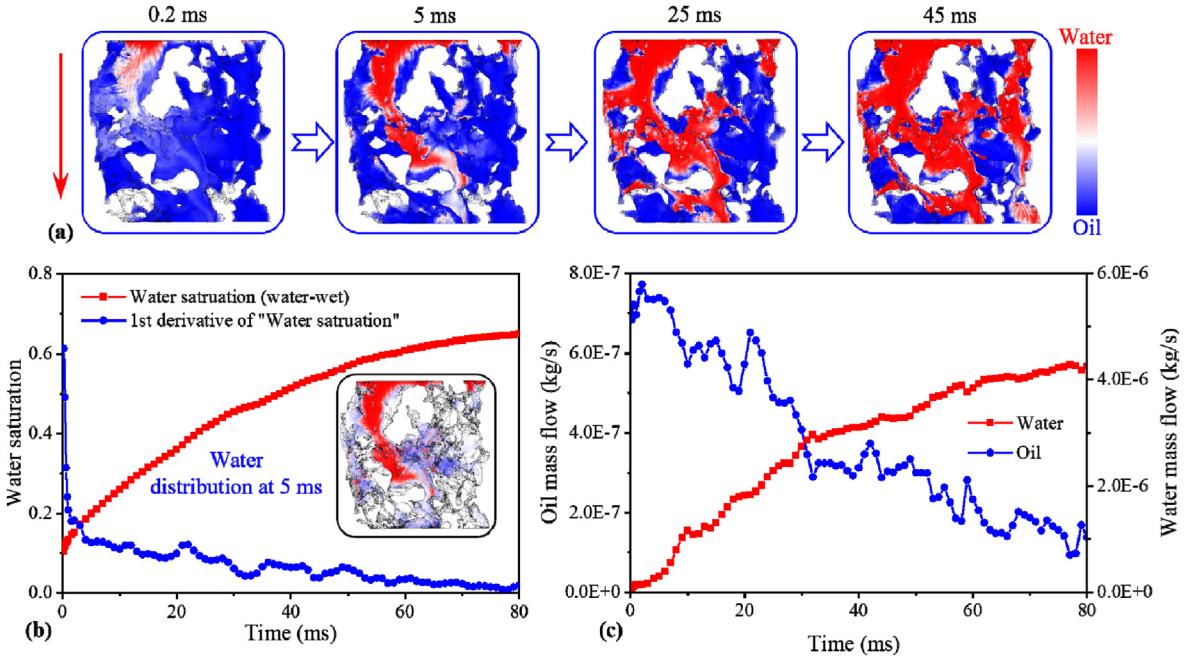

Fig. 7. Dynamic water flooding process under water-wet condition: (a) Water-oil volume fraction distribution; (b) Water saturation as a function of displacement time and its first derivative; and (c) Dynamic water-oil mass flow.

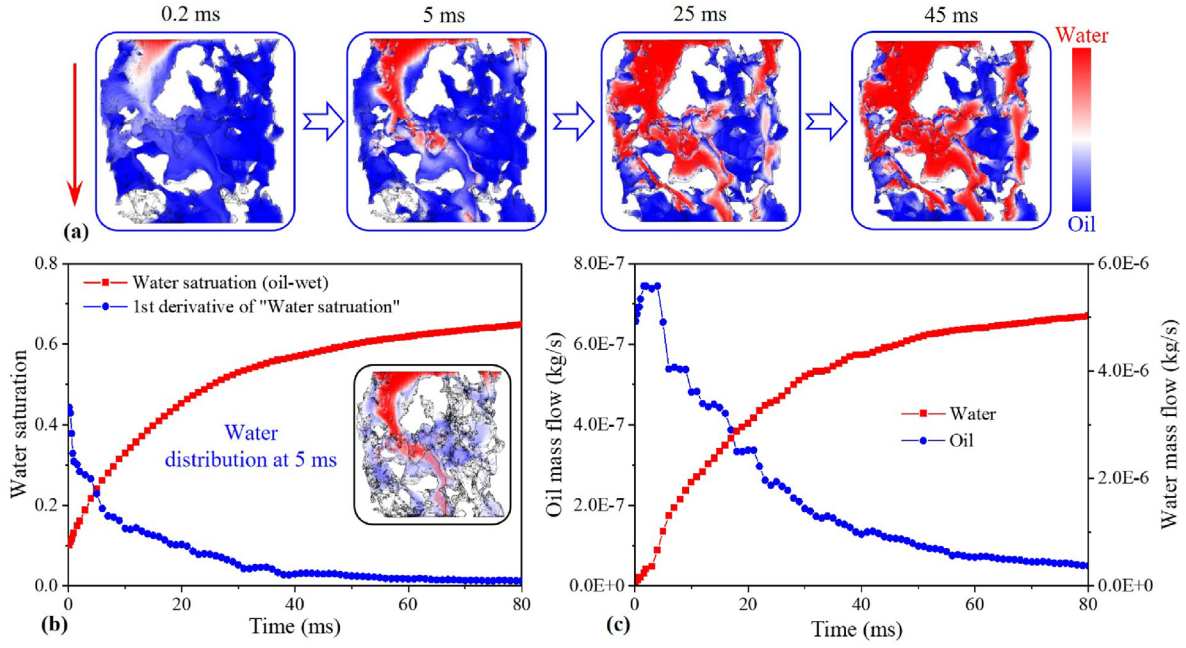

Fig. 8. Dynamic water flooding process under oil-wet condition: (a) Water-oil volume fraction distribution; (b) Water saturation as a function of displacement time and its first derivative; and (c) Dynamic water-oil mass flow.

The effect of pore-throat structures on water flooding is further analyzed according to the microscopic simulation results. Fig. 9a displays the water distribution in the pore-throat system, indicating that three displacement channels are formed during the water flooding, defined as channels 1, 2, and 3 (see Fig. 9b). The displacement sequence is the same under different wetting conditions; i.e. channel 1 is displaced first, then channel 2, and finally channel 3. Specifically, there are two narrow throats in the displacement channels (#1 and #2, as displayed in Fig. 9b); channels 1 and 2 share a flow channel near the inlet, and there is a narrow throat in channel 2 after bifurcation. Accordingly, the injected water first breaks through the outlet along channel 1 and then through channel 2. While the water in channel 3 breaks through the outlet at the latest due to its small size and the existence of a narrow throat. Fig. 9c illustrates the water-oil distribution after flooding in two narrow throats under water-wet and oil-wet conditions. Obviously, the flow channels widen rapidly as the fluid passes through the narrow throats. The water flooding has a

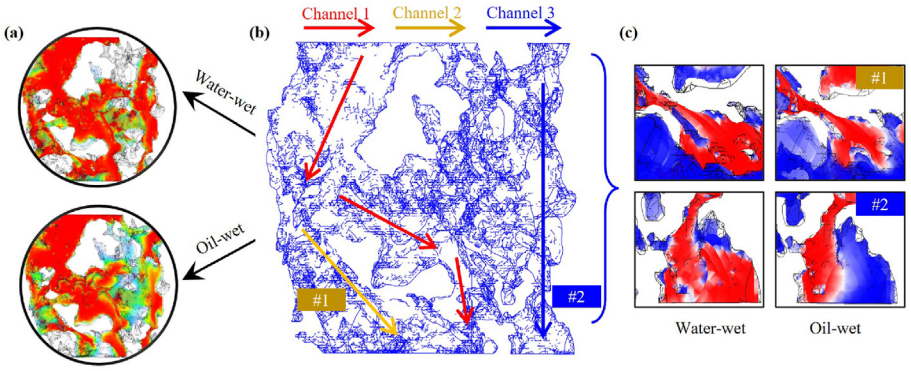

Fig. 9. Influence mechanism of pore-throat structure on water flooding under water-wet and oil-wet conditions: (a) Water phase distribution in the pore-throat system; (b) Dominant displacement channels; and (c) Effect of the narrow throat on water flooding.

better performance in this case under the water-wet condition since water gradually displaces oil along hydrophilic pore-throat surfaces with a wide displacement range; whereas in the oil-wet system, water prefers to flow sandwiched in oil due to hydrophobic pore-throat surfaces, forming a thick oil film. Thus, the displacement performance is dissatisfactory.

After the water breaks through the outlet along the dominant channels, it takes a long time to reach the equilibrium state. Thus, the final time of the iterative calculation is set to 80 ms. The residual oil saturation in water-wet and oil-wet systems is 0.3502 and 0.3515, respectively. According to the analysis results of Figs. 7 and 8, water flooding in the water-wet system takes a longer time to reach equilibrium due to the effect of imbibition. Therefore, the residual oil saturation in the water-wet system should be lower. Fig. 10 displays the oil distribution after iterative calculation, indicating that there is a large amount of residual oil in poorly connected pores. Besides, the flooding range is extensive, and the residual oil is mainly distributed in dead-end pores due to the trapping scenario in the water-wet system; while the residual oil is mainly distributed as oil films on rough pore-throat surfaces in the oil-wet system, and thick oil films are found in poorly connected pores.

4.3. Macroscopic relative permeability modeling for the effects of wettability and microporosity

The water-oil relative permeability simulations under different wetting conditions (oil-wet pores fractions were 0, 0.25, 0.5, 0.75 and 1, respectively.) and microporosity (0, 0.25, 0.5, 0.75, 1) were performed using the quasi-static PNM. Microporosity significantly affects the drainage and water flooding process, while wettability only affects water flooding since the pore-throat system is water-wet in the drainage process.

The water relative permeability gradually decreases, and the oil relative permeability increases during the drainage (see Fig. 11a). The variation of water-oil relative permeability is significant when the microporosity is 1, and it gradually weakens with the decrease of microporosity. This is because the initial pore-throat system is hydrophilic, and the capillary pressure of the micropores is the resistance to drainage. Furthermore, there is a positive linear correlation between microporosity and residual water saturation (see Fig. 11b), indicating the larger the microporosity, the lower the invading oil volume fraction.

The pore-throat system may be water-wet, oil-wet, and mixed-wet after the drainage. Both microporosity and wettability significantly affect water flooding. The simulation results show that wettability similarly affects water-oil relative permeability under different micro-porosities. The relative permeability curves with a microporosity of 0 and oil-wet pores fractions of 0–1 are displayed in Fig. 12a. The water relative permeability increases, while the oil relative permeability decreases gradually during water flooding. However, due to the narrow pore-throat structures (see Fig. 6) and the altered wettability of the PNM, the water relative permeability is low. The oil relative permeability decreases the fastest when the oil-wet pores fraction is 1, and the water relative permeability is 0.094 at the end of the displacement, which is the highest under all wetting conditions. In contrast, the oil relative permeability decreases slowly under the water-wet condition, and the water

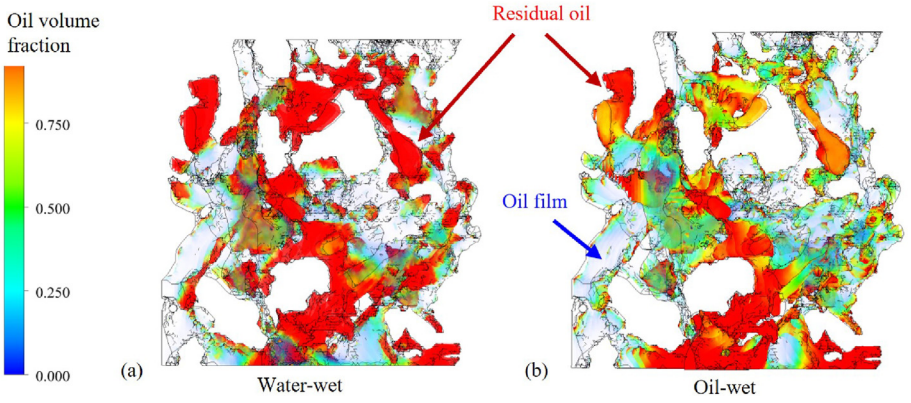

Fig. 10. Residual oil distribution in water-wet and oil-wet conditions: (a) Water-wet system and (b) Oil-wet system.

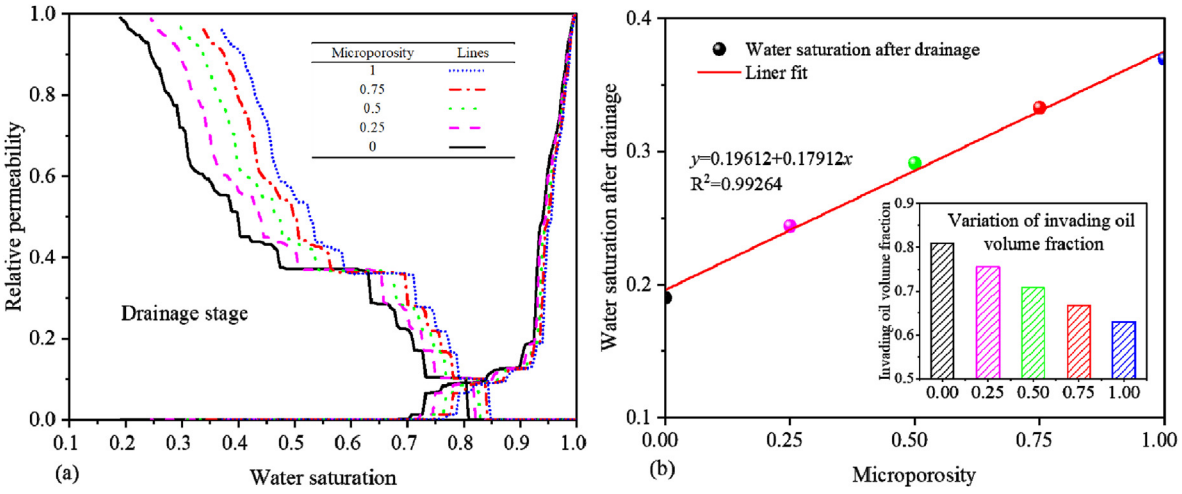

Fig. 11. Effect of microporosity on drainage: (a) Variation of water-oil relative permeability; and (b) Residual water saturation.

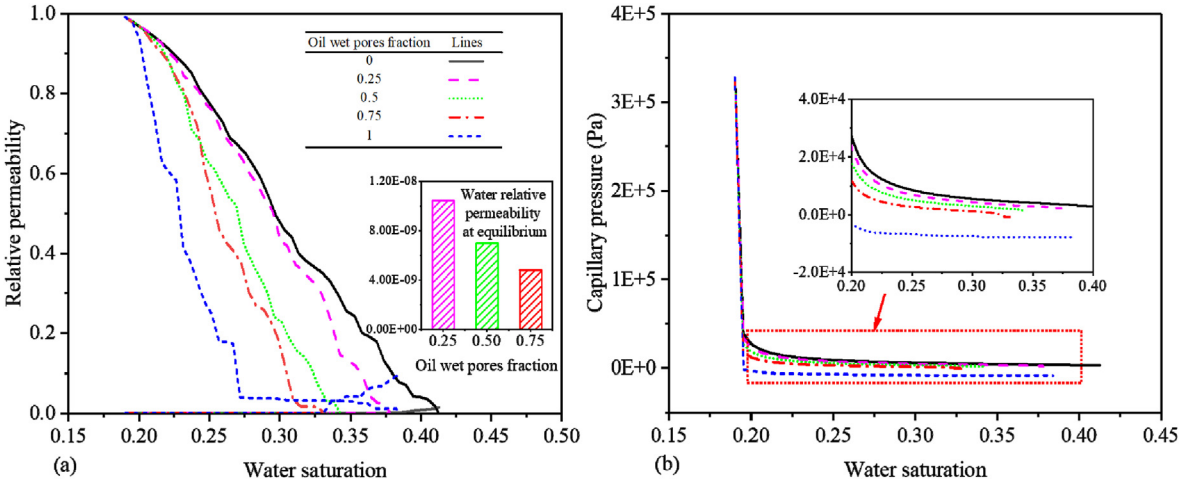

Fig. 12. Water flooding process when the microporosity is 0: (a) Water-oil relative permeability; and (b) Capillary pressure.

relative permeability is 0.015 at the end of the displacement. While the water relative permeability is extremely low, and the oil relative permeability varies significantly under mixed wetting conditions; besides, the final water relative permeability decreases with increasing oil-wet pores fraction. Fig. 12b illustrates that the capillary pressure decreases during water flooding. The capillary pressure is positive and acts as a driving force in the water-wet system. The larger the oil-wet pores fraction, the lower the capillary pressure due to the capillary resistance within the oil-wet pores.

The effect of microporosity and wettability on residual oil saturation is further evaluated (see Fig. 13a). It is found that large microporosity corresponds to low residual oil saturation, and there is a negative linear correlation between microporosity and residual oil saturation under different wettability conditions. For the effect of wettability, the residual oil saturation is lower under the water-wet condition, followed by the oil-wet condition. Besides, it increases with the increasing oil-wet pores fraction under mixed-wetting conditions. The residual oil saturation is the lowest when the oil-wet pores fraction is 0 and the microporosity is 1. The volume fraction of displaced oil is obtained from the difference between water saturation after flooding and drainage (see Fig. 13b); it first decreases and then increases with the increasing oil-wet pores fraction. The volume fraction of displaced oil is the largest when the pore-throat system is water-wet, followed by the oil-wet condition. The microporosity is negatively correlated with the volume fraction of displaced oil. The volume fraction of displaced oil is the largest when the microporosity and oil-wet pores fraction are both 0.

The effect mechanisms of microporosity and wettability on water-oil flow are displayed in Fig. 14. Micropores are mainly distributed around pore spaces (see Fig. 14a). Water in the micropores cannot be drained during the drainage due to hydrophilic pore surfaces, so the microporosity is positively correlated with the residual water saturation (see Fig. 7). Besides, injected water preferentially contacts the residual water in the micropores during flooding, and it flows along the developed micropores and gradually displaces the oil in pore spaces. Thus, the larger the microporosity, the lower the residual oil saturation (see Fig. 13a). However, the microporosity is inversely proportional to the volume fraction of displaced oil (see Fig. 13b), because the PNM with high microporosity limits the invasion of oil during drainage (see Fig. 11).

Regarding the effect of wettability on water flooding, the variation of relative permeability can be well explained through microscopic water-oil displacement mechanisms. Specifically, water easily flows along pore surfaces and displaces oil with a lower mass flow due to hydrophilic surfaces under the water-wet

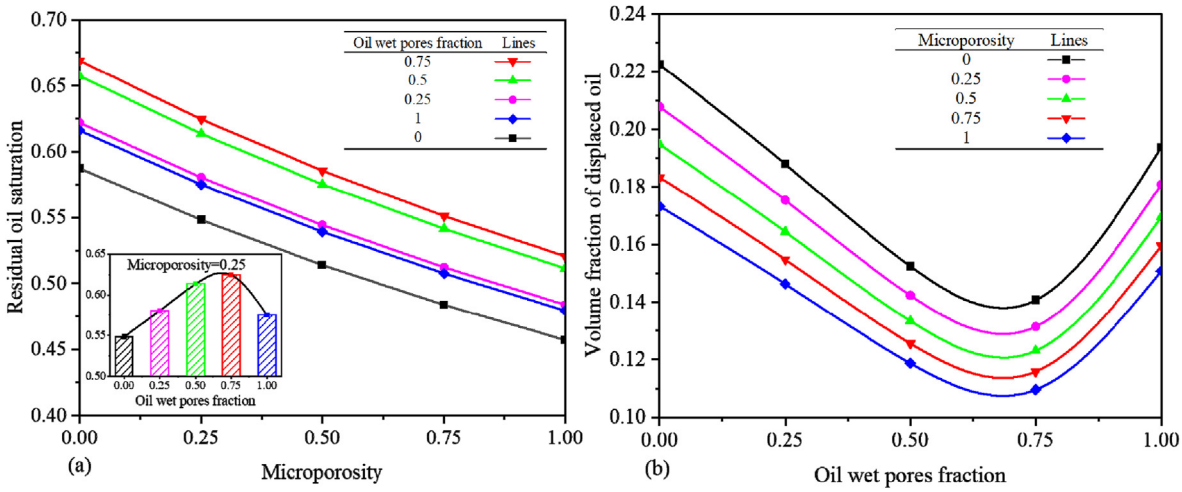

Fig. 13. Effects of microporosity and wettability on displacement: (a) Effect on residual oil saturation; and (b) Effect on the volume fraction of displaced oil.

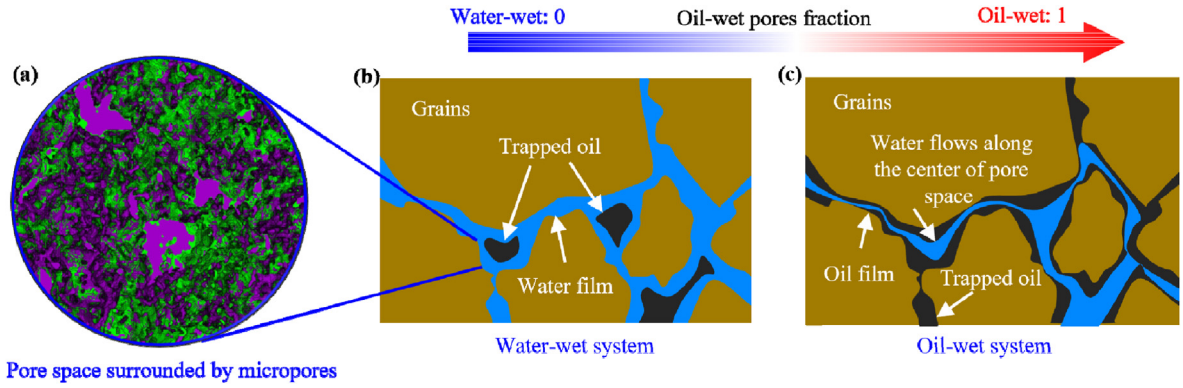

Fig. 14. Influence mechanism of micropores and wettability on water-oil flow: (a) Spatial distribution of micropores; (b) Water-oil flow in the water-wet system; and (c) Water-oil flow in the oil-wet system.

condition (see Fig. 7); while water is sandwiched in oil and breaks through the outlet earlier with a large mass flow due to the hydrophobic pore-throat surface (see Fig. 8). Therefore, the variation of water-oil relative permeability is significant, and the water relative permeability is high under the oil-wet condition (see Fig. 12). For displacement efficiency, the water flooding performs better under water-wet condition due to the wide displacement range and low residual oil saturation (see Figs. 9 and 10). This is consistent with the macroscopic modeling results (see Fig. 13). Under the water-wet condition, the injected water displaces oil along hydrophilic surfaces, which may lead to oil trapped in poorly connected and dead-end pores (see Fig. 14b). In addition, the trapped oil is also related to connectivity and pore-throat size. The stronger the connectivity, the larger the throat size, and the easier the oil escapes according to the Jamin effect. In contrast, oil trapping does not occur in the oil-wet system. Nevertheless, there is an oil film on pore-throat surfaces, which severely limits the displacement range (see Fig. 14c).

The water-oil mass flow and volume fraction distribution obtained by microscopic modeling results correspond to the analysis results of quasi-static PNM under water-wet and oil-wet conditions, verifying the rationality of the comprehensive modeling method. Moreover, the displacement efficiency under mixed wetting conditions is further evaluated by PNM, which is lower due to poor water connectivity. The injected water flows along the micropores and the discontinuous water films on pore surfaces, resulting in lower water relative permeability and flooding efficiency. The effect of oil-wet pores fraction on residual oil saturation in Fig. 13 roughly corresponds to the findings of Gharbi and Blunt (2012). Due to the difference in pore structure properties and connectivity of low permeability porous media, the turning point is larger. However, this work further elucidates the effect of microporosity on water-oil flow.

5. Conclusions

This work studied water-oil flow in low permeability porous media by constructing a free surface model for microscopic dynamic water flooding and a dual porosity quasi-static PNM for water-oil relative permeability. The effects of pore structure properties and wettability on displacement efficiency are studied. The following conclusions are drawn:

(1) The pore structures of the microscopic and macroscopic models are significantly different since the pore-throat distribution in macroscopic models is regular, while the large-diameter pores are randomly distributed in microscopic models. This means that macroscopic models represent the properties of scanned samples, while the microscopic models reflect system heterogeneity.
(2) The microscopic displacement mechanisms explain the corresponding relative permeability. In the oil-wet system, the

water entrained in oil breaks through the outlet earlier with a large mass flow, resulting in significant changes in water-oil relative permeability. In the water-wet system, water slowly displaces oil along hydrophilic pore surfaces and continues to displace oil by imbibition. Therefore, the oil relative permeability decreases slowly, and the water relative permeability is lower. Under mixed wetting conditions, the water relative permeability is extremely low due to the poor connectivity of water.

(3) The residual oil saturation is low in the water-wet system; water displaces oil extensively for the positive effect of capillary pressure, and residual oil is mainly trapped in poorly connected pores. While thick oil films exist in rough pore surfaces and poorly connected pores for capillary resistance in the oil-wet system. In addition, the residual oil saturation is high for poor flooding efficiency in mixed wetting systems.

(4) For the effect of pore structure properties, the narrow throats affect the flooding sequence and limits flooding range in the oil-wet system. Besides, the invading oil volume fraction negatively correlates with microporosity during drainage. A large microporosity corresponds to low residual oil saturation. Nevertheless, the volume fraction of displaced oil is smaller.

Declaration of competing interest

The authors declare that they have no known competing financial interests or personal relationships that could have appeared to influence the work reported in this paper.

Acknowledgments

This work was supported by National Natural Science Foundation of China (Grant No. 42172159), and Science Foundation of China University of Petroleum, Beijing (Grant No. 2462023XKBH002).

References

Ambekar, A.S., Mattey, P., Buwa, V.V., 2021. Pore-resolved two-phase flow in a pseudo-3D porous medium: measurements and volume-of-fluid simulations. Chem. Eng. Sci. 230, 116128.
Bashir, A., Sharifi Haddad, A., Rafati, R., 2022. A review of fluid displacement mechanisms in surfactant-based chemical enhanced oil recovery processes: analyses of key influencing factors. Pet. Sci. 19 (3), 1211–1235.
Basirat, F., Yang, Z., Niemi, A., 2017. Pore-scale modeling of wettability effects on CO_2–brine displacement during geological storage. Adv. Water Resour. 109, 181–195.
Blunt, M.J., 1997. Pore level modeling of the effects of wettability. SPE J. 2 (4), 494–510.
Brackbill, J.U., Kothe, D.B., Zemach, C., 1992. A continuum method for modeling surface tension. J. Comput. Phys. 100 (2), 335–354.
Cai, J., Jin, T., Kou, J., et al., 2021. Lucas–Washburn equation-based modeling of capillary-driven flow in porous systems. Langmuir 37 (5), 1623–1636.
Carrillo, F.J., Soulaine, C., Bourg, I.C., 2022. The impact of sub-resolution porosity on numerical simulations of multiphase flow. Adv. Water Resour. 161, 104094.
Chen, J., Cheng, W., Wang, G., Li, H., Li, Y., 2021. New method of monitoring the transmission range of coal seam water injection and correcting the monitoring results. Measurement 177, 109334.
Chen, L., He, A., Zhao, J., et al., 2022. Pore-scale modeling of complex transport phenomena in porous media. Prog. Energy Combust. Sci. 88, 100968.
Cui, J., Yuan, X., Wu, S., et al., 2021. Rock types and reservoir characteristics of Shahejie formation Marl in Shulu Sag, Jizhong depression, Bohai Bay Basin. J. Earth Sci. 32 (4), 986–997.
Gharbi, O., Blunt, M.J., 2012. The impact of wettability and connectivity on relative permeability in carbonates: a pore network modeling analysis. Water Resour. Res. 48 (12), W12513.
Hao, Y., Li, Z., Su, Y., et al., 2022. Experimental investigation of CO_2 storage and oil production of different CO_2 injection methods at pore-scale and core-scale. Energy 254, 124349.
Hashemi, L., Blunt, M., Hajibeygi, H., 2021. Pore-scale modelling and sensitivity analyses of hydrogen-brine multiphase flow in geological porous media. Sci. Rep. 11 (1), 8348.
Hu, C., Liu, X., Jia, Y., Duan, Z., 2020. Permeability anisotropy of methane hydrate-bearing sands: insights from CT scanning and pore network modelling. Comput. Geotech. 123, 103568.
Hu, R., Wan, J., Yang, Z., Chen, Y.-F., Tokunaga, T., 2018. Wettability and flow rate impacts on immiscible displacement: a theoretical model. Geophys. Res. Lett. 45 (7), 3077–3086.
Idowu, N., Long, H., Øren, P.E., et al., 2015. Wettability analysis using micro-CT, FESEM and QEMSCAN, and its applications to digital rock physics. In: Proceedings of the International Symposium of the Society of Core Analysts. SCA2015-010.
Ju, Y., Gong, W., Chang, W., Sun, M., 2020. Effects of pore characteristics on water-oil two-phase displacement in non-homogeneous pore structures: a pore-scale lattice Boltzmann model considering various fluid density ratios. Int. J. Eng. Sci. 154, 103343.
Lin, Q., Bijeljic, B., Foroughi, S., Berg, S., Blunt, M.J., 2021a. Pore-scale imaging of displacement patterns in an altered-wettability carbonate. Chem. Eng. Sci. 235, 116464.
Lin, W., Xiong, S., Liu, Y., et al., 2021b. Spontaneous imbibition in tight porous media with different wettability: pore-scale simulation. Phys. Fluids 33 (3), 032013.
Liu, T., Wang, M., 2022. Critical REV size of multiphase flow in porous media for upscaling by pore-scale modeling. Transport Porous Media 144, 111–132.
Liu, C., Zhang, L., Li, Y., et al., 2022a. Effects of microfractures on permeability in carbonate rocks based on digital core technology. Adv. Geo-Energy Res. 6 (1), 86–90.
Liu, Y., Chen, M., Sun, S., et al., 2022b. Effects of grain shape and packing pattern on spontaneous imbibition under different boundary conditions: pore-scale simulation. J. Hydrol. 607, 127484.
Mascini, A., Boone, M., Van Offenwert, S., et al., 2021. Fluid invasion dynamics in porous media with complex wettability and connectivity. Geophys. Res. Lett. 48 (22), e2021GL095185.
McClure, J.E., Li, Z., Berrill, M., Ramstad, T., 2021. The LBPM software package for simulating multiphase flow on digital images of porous rocks. Comput. Geosci. 25 (3), 871–895.
Øren, P.E., Bakke, S., Arntzen, O.J., 1998. Extending predictive capabilities to network models. SPE J. 3 (4), 324–336.
Qiao, J., Zeng, J., Chen, D., et al., 2022. Permeability estimation of tight sandstone from pore structure characterization. Mar. Pet. Geol. 135, 105382.
Qin, C., van Brummelen, H., Hefny, M., Zhao, J., 2021. Image-based modeling of spontaneous imbibition in porous media by a dynamic pore network model. Adv. Water Resour. 152, 103932.
Qin, X., Xia, Y., Wu, J., et al., 2022. Influence of pore morphology on permeability through digital rock modeling: new insights from the Euler number and shape factor. Energy Fuel. 36 (14), 7519–7530.
Shan, L., Bai, X., Liu, C., et al., 2022. Super-resolution reconstruction of digital rock CT images based on residual attention mechanism. Adv. Geo-Energy Res. 6 (2), 157–168.
Siavashi, J., Najafi, A., Ebadi, M., Sharifi, M., 2022. A CNN-based approach for upscaling multiphase flow in digital sandstones. Fuel 308, 122047.
Wang, Y., Sun, S., 2021. Multiscale pore structure characterization based on SEM images. Fuel 289, 119915.
Wang, G., Qin, X., Han, D., Liu, Z., 2021. Study on seepage and deformation characteristics of coal microstructure by 3D reconstruction of CT images at high temperatures. Int. J. Min. Sci. Technol. 31 (2), 175–185.
Wang, G., Chen, X., Wang, S., Chen, H., 2022. Influence of fracture connectivity and shape on water seepage of low-rank coal based on CT 3D reconstruction. J. Nat. Gas Sci. Eng. 102, 104584.
Wang, S., Chen, L., Feng, Q., et al., 2023. Pore-scale simulation of gas displacement after water flooding using three-phase lattice Boltzmann method. Capillarity 6 (2), 19–30.
Xu, F., Liang, S., Zhang, Y., Li, B., Hu, Y., 2021a. Numerical study of water–air distribution in unsaturated soil by using lattice Boltzmann method. Comput. Math. Appl. 81, 573–587.
Xu, Z., Lin, M., Jiang, W., Ji, L., Cao, G., 2021b. Rapid multiscale pore network modeling for drainage in tight sandstone. J. Pet. Sci. Eng. 204, 108682.
Yan, G., Li, Z., Bore, T., et al., 2022. A lattice Boltzmann exploration of two-phase displacement in 2D porous media under various pressure boundary conditions. J. Rock Mech. Geotech. Eng. 14 (6), 1782–1798.
Yang, Y., Wang, K., Zhang, L., et al., 2019. Pore-scale simulation of shale oil flow based on pore network model. Fuel 251, 683–692.
Yang, Y., Cai, S., Yao, J., et al., 2021. Pore-scale simulation of remaining oil distribution in 3D porous media affected by wettability and capillarity based on volume of fluid method. Int. J. Multiphas. Flow 143, 103746.
Zhang, L., Ge, K., Wang, J., Zhao, J., Song, Y., 2020. Pore-scale investigation of permeability evolution during hydrate formation using a pore network model based on X-ray CT. Mar. Pet. Geol. 113, 104157.
Zhang, T., Zhang, L., Zhao, Y., et al., 2022a. Ganglia dynamics during imbibition and drainage processes in nanoporous systems. Phys. Fluids 34 (4), 042016.
Zhang, W., Feng, Q., Wang, S., et al., 2022b. Pore network modeling of oil and water transport in nanoporous shale with mixed wettability. J. Pet. Sci. Eng. 209, 109884.
Zhao, B., MacMinn, C.W., Juanes, R., 2016. Wettability control on multiphase flow in patterned microfluidics. Proc. Natl. Acad. Sci. U. S. A. 113 (37), 10251–10256.

Zhao, B., MacMinn, C.W., Primkulov, B.K., et al., 2019. Comprehensive comparison of pore-scale models for multiphase flow in porous media. Proc. Natl. Acad. Sci. U. S. A. 116 (28), 13799–13806.
Zhao, J., Qin, F., Derome, D., Carmeliet, J., 2020. Simulation of quasi-static drainage displacement in porous media on pore-scale: coupling lattice Boltzmann method and pore network model. J. Hydrol. 588, 125080.
Zheng, H., Cao, S., Yuan, W., et al., 2022. A time-dependent hydro-mechanical coupling model of reservoir sandstone during CO_2 geological storage. Rock Mech. Rock Eng. 55, 5845–5861.

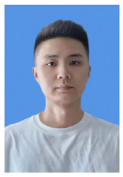

Xiangjie Qin is pursuing his PhD at China University of Petroleum, Beijing. He received bachelor's and master's degrees in Shandong University of Science and Technology, China, in 2018 and 2021, respectively. He is interested in pore structure characterization and fluid transport mechanisms of low permeability reservoirs, digital rock reconstruction and analysis, pore scale numerical simulation of imbibition and multiphase flow.